

GRB Cosmology and Self-organized Criticality in GRBs

F. Y. Wang^{*†}

School of Astronomy and Space Science, Nanjing University

E-mail: fayinwang@nju.edu.cn

Gamma-ray bursts (GRBs), which have isotropic energy up to 10^{54} erg, would be the ideal tool to study the properties of early universe: including dark energy, star formation rate, and the metal enrichment history of the Universe. We will briefly review the progress on the field of GRB cosmology. Meanwhile, X-ray flares, which may have important clues to the central engine, are common phenomena in the GRB afterglows. We present statistical results of X-ray flares, i.e., energy, duration time and waiting time distributions, and compare the results with solar flares. The similarity between the two kinds of flares are found, which may indicates that the physical mechanism of GRB X-ray flares is magnetic reconnection.

*Swift: 10 Years of Discovery,
2-5 December 2014
La Sapienza University, Rome, Italy*

^{*}Speaker.

[†]A footnote may follow.

1. Introduction

The accelerating Universe at the present epoch was discovered from the observation of type Ia supernovae (SNe Ia) [1, 2]. The cosmic accelerated expansion has also been confirmed by other observations, such as cosmic microwave background (CMB) [3], and large-scale structure (LSS) [4]. But the SNe Ia can only be detected at low redshifts, i.e., $z < 2.0$. Gamma-ray bursts (GRBs), as the most powerful explosions in the Universe [5, 6], can fill the gap between SNe and CMB. GRBs can serve as the complementary tools to measure dark energy and cosmic expansion [7, 8, 9, 10, 11, 12]. Long GRBs can be made “relative standard candles”, using luminosity correlations that have been found in prompt and afterglow phases [9, 13, 14].

X-ray flares with short rise and decay times are discovered by Swift satellite. The isotropic-equivalent energy of X-ray flares is from $\sim 10^{48}$ to 10^{52} erg. The occurrence times of X-ray flares range from a few seconds to 10^6 seconds after the GRB trigger. Until now, the physical origin of X-ray flares has remained mysterious, although some models have been proposed. Here we investigate the energy release frequency distribution, duration-time frequency distribution and waiting time distribution of GRB X-ray flares [15]. On the other hand, it is well known that solar flare is triggered by a magnetic reconnection process. So we will compare these two kind of flares.

2. Constraints on dark energy

GRBs have been widely used to constrain dark energy. We use the calibrating method to standardize 151 long GRBs with $E_{\text{iso}} - E_p$ correlation. Just as using Cepheid variables to standardize SNe Ia, the GRBs can be calibrated with SNe Ia. We use the latest Union 2.1 data. This method is also cosmological model-independent [16]. The full GRB data is separated into two groups. The dividing line is the highest redshift in SNe Ia Union 2.1 data, namely $z = 1.414$. The low-redshift group ($z < 1.414$) includes 61 GRBs, and the high-redshift group ($z > 1.414$) contains 90 GRBs. The left panel of Figure 1 shows the 1σ and 2σ constraints on the $\Omega_m - \Omega_\Lambda$ plane. Adding the GRB data can give much more tighter constraints.

We also use the nonparametric technique to constrain the uncorrelated equation of state (EOS) of dark energy $w(z)$. The EOS is the most important parameters of dark energy. We apply the nonparametric method to a joint data set of the latest observations including SNe Ia, CMB from Planck and WMAP polarization, large scale structure, the Hubble parameter measurement and GRBs. The right panel of Figure 1 shows the evolution of uncorrelated EOS of dark energy, which is consistent with Λ CDM at the 2σ confidence level [17].

3. Star formation rate

The high-redshift star formation rate (SFR) is important in many fields in astrophysics. Direct SFR measurement is still out of reach by present instruments, particularly at the faint end of the galaxy luminosity function. Long GRBs triggered by the death of massive stars, provide a complementary technique for measuring the SFR. In order to test the GRB rate relative to the SFR, we must choose bursts with high luminosities, because only bright bursts can be seen at low and high-redshifts, so we choose the luminosity cut $L_{\text{iso}} > 10^{51}$ erg s^{-1} [18] in the redshift bin $0 - 4$.

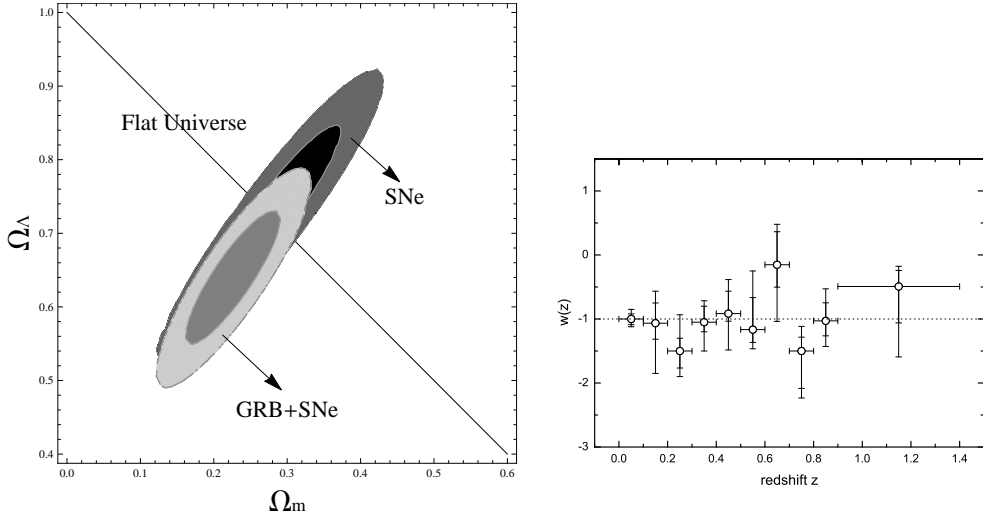


Figure 1: Left: 1σ and 2σ constraints on Ω_m and Ω_Λ from different data sets. The solid line shows the $\Omega_k = 0$ case. Right: Estimation of the uncorrelated dark energy EOS parameters at different redshift bins (w_1, w_2, \dots, w_{10}) from SNe Ia+BAO+WMAP9+H(z) data. The open points show the best fit value. The error bars are 1σ and 2σ confidence levels. The dotted line shows the cosmological constant. Adopted from [17].

This removes many low-redshift, low- L_{iso} bursts that could not have been seen at higher redshift. The SFR can be estimated as

$$\langle \dot{\rho}_* \rangle_{z_1-z_2} = \frac{N_{z_1-z_2}^{\text{obs}}}{N_{1-4}^{\text{obs}}} \frac{\int_1^4 dz \frac{dV_{\text{com}}/dz}{1+z} (1+z)^\delta \dot{\rho}_*(z)}{\int_{z_1}^{z_2} dz \frac{dV_{\text{com}}/dz}{1+z} (1+z)^\delta}, \quad (3.1)$$

where $N_{z_1-z_2}^{\text{obs}}$ is the observed GRB counts, and $\delta = 0.5$ [19]. The derived SFR from GRBs are shown as filled circles in the left panel of Figure 2. Error bars correspond to 68% Poisson confidence intervals for the binned events. The high-redshift SFRs obviously decrease with increasing redshifts, although an oscillation may exist. We find that the SFR at $z > 4.48$ is proportional to $(1+z)^{-3}$ using minimum χ^2 method, which is shown as solid line in Figure 2. The right panel shows the optical depth τ_e due to the scattering between the ionized gas and the CMB photons. The WMAP nine-year data gives $\tau_e = 0.089 \pm 0.014$ [20], which is shown as the shaded region. So our GRB-inferred SFR can reproduce the CMB optical depth.

4. Pop III GRBs and metal enrichment

Absorption lines on the spectra of bright background sources, such as, are main sources of information about the chemical properties of high-redshift universe [21]. We simulate the formation of first galaxy. When a GRB explodes, its light will go through the metal-polluted region, so absorption line will appear in the spectrum. We found that the metals in the first galaxies produced by the first supernova explosion are likely to reside in low ionization states (C II, O I, Si II and Fe II). The GRB afterglow travel through the polluted environment in the first galaxy. The metals will produce the metal absorption lines in the GRB spectrum, as shown in Figure 4. Because the

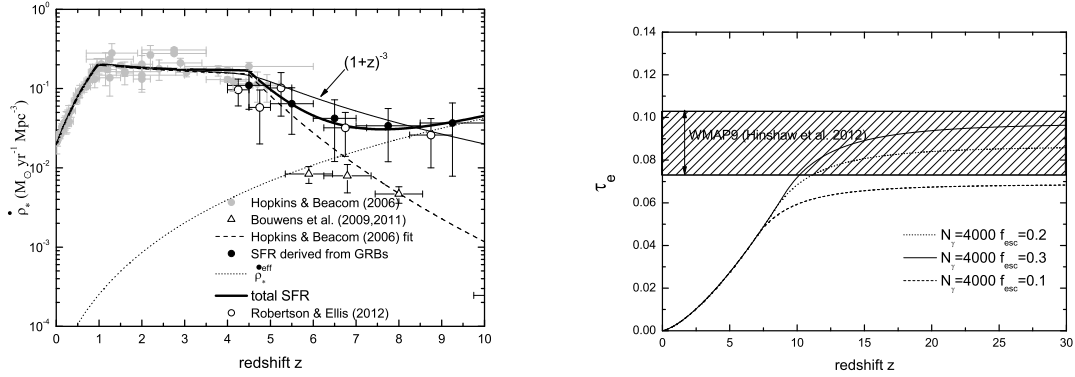
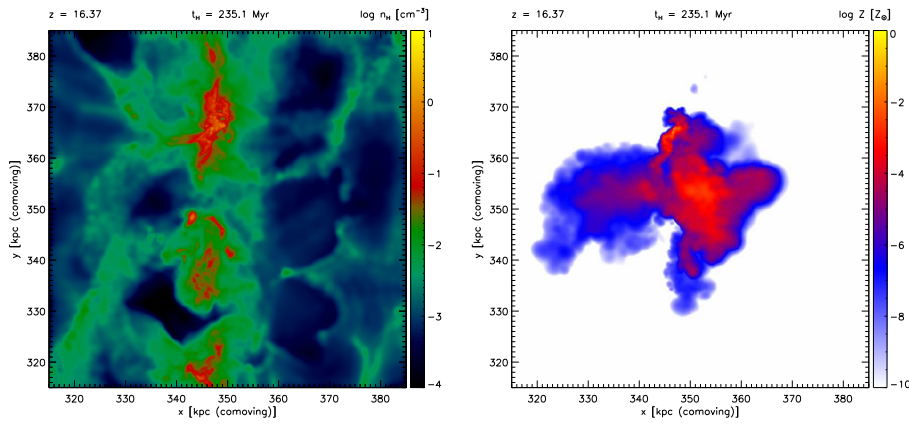


Figure 2: The cosmic star formation history. The dashed line shows their fitting result. The filled circles are the SFR derived from GRBs in this work. Adopted from Wang (2014).



(a)

Figure 3: Possible explosion sites for Pop III bursts. Shown are the hydrogen number density and metallicity contours during the assembly of a first galaxy, averaged along the line of sight within the central $\simeq 100$ kpc (comoving), at $z \simeq 16.4$, closer to the virialization of the atomic cooling halo. Now, metals are being re-assembled into the growing potential well of the first galaxy. The topology of metal enrichment is highly inhomogeneous, with pockets of highly enriched material embedded in regions with a largely primordial composition. Adopted from [22].

topology of metal enrichment could be highly inhomogeneous, so along different lines of sight, the metal absorption lines may show a distinct signature. The metal absorption lines, in terms of their flux density and corresponding equivalent widths, will be detectable in the near future, with the launch of the JWST. From Figure 4, we can distinguish whether the Pop III progenitor dies as PISN, or Type II supernova from the observation of Pop III GRBs spectrum [22].

5. Self-organized criticality in GRBs

Thanks to the rapid-response capability and high sensitivity of the Swift satellite, numerous

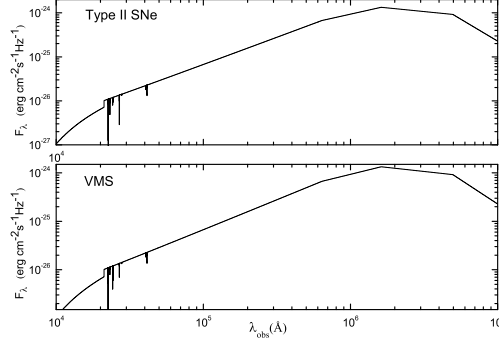


Figure 4: The total GRB spectrum with the metal absorption lines at the reverse shock crossing time ($t_{\oplus} = 16.7 \times (1 + 16.37)s$). Adopted from [22].

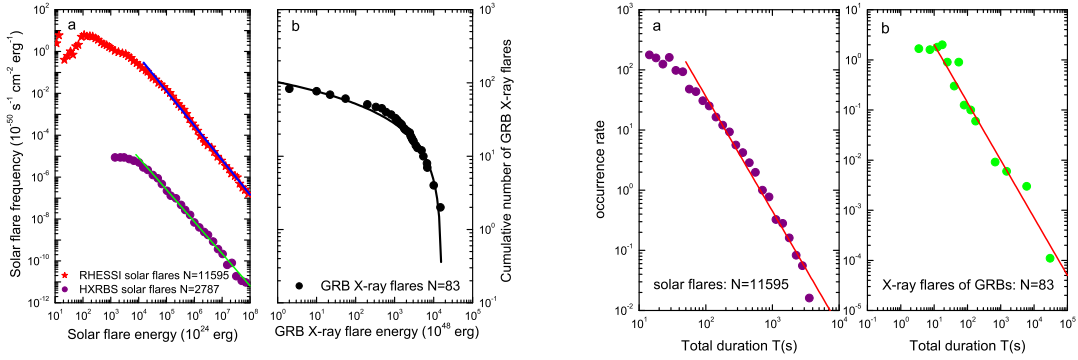


Figure 5: Left: Energy-release frequency distributions. a, The differential energy frequency distribution of solar hard X-ray flares. **b,** The cumulative energy distribution of GRB X-ray flares. The 83 GRB X-ray flares are shown as black dots. The black curve gives the cumulative energy distribution $N(> E) = a + b[E^{1-\alpha_E} - E_{\max}^{1-\alpha_E}]$ with $\alpha_E \sim 1.06 \pm 0.15$ for GRB X-ray flares. **Right: Duration-time frequency distributions. a,** The relation between the occurrence rate and duration time for solar flares. **b,** The relation between the occurrence rate and duration time for GRB X-ray flares shown as green dots. Adopted from [15].

unforeseen features have been discovered, one of which is that about half of bursts have large, late-time X-ray flares with short rise and decay times. The unexpected X-ray flares with an isotropic-equivalent energy from 10^{48} to 10^{52} ergs have been detected for both long and short bursts. We find that X-ray flares and solar flares share three statistical properties: power-law frequency distributions for energies (left panel of Figure 5), durations (right panel of Figure 5), and waiting times, which can be explained by self-organized criticality (SOC) theory [15]. Guidorzi et al. (2015) found that the waiting time distributions of gamma-ray pulses and X-ray flares of GRBs also had power-law tail extending over four decades, which can be understood by SOC theory [23]. For a SOC system [24, 25, 26], owing to some driving force, subsystems will self-organize to a critical state at which a small perturbation can trigger an avalanche-like chain reaction of any size within the system. The

two types of flares are driven by a magnetic reconnection process.

6. Conclusions

GRBs are promising tools for studying the properties of early Universe, including dark energy, star formation rate and metal enrichment history. In the future, the French-Chinese satellite Space-based multi-band astronomical Variable Objects Monitor (SVOM) and JWST, have been optimized to increase the number of GRB and the synergy with the ground-based facilities. This will open a new window of the dark ages of the Universe.

References

- [1] Riess, A. G., et al., 1998, *AJ*, 116, 1009
- [2] Perlmutter, S., et al., 1999, *ApJ*, 517, 565
- [3] Komatsu, S., et al., 2011, *ApJS*, 192, 18
- [4] Eisenstein, D. J., et al., 2005, *ApJ*, 633, 560
- [5] Zhang, B., & Meszaros, P., 2004, *IJMPA*, 19, 2385
- [6] Wang, F. Y., Dai, Z. G. & Liang, E. W., 2015, *New Astronomy Reviews*, 67, 1
- [7] Dai, Z. G., Liang, E. W. & Xu, D., 2004, *ApJ*, 612, L101
- [8] Ghirlanda, G., et al., 2004, *ApJ*, 613, L13
- [9] Liang, E. W. & Zhang, B., 2005, *ApJ*, 633, 611
- [10] Amati, L., et al., 2008, *MNRAS*, 391, 577
- [11] Wang, F. Y. & Dai, Z. G., 2011, *A&A*, 536, A96
- [12] Wang, F. Y., Qi, S. & Dai, Z. G., 2011, *MNRAS*, 415, 3423
- [13] Amati, L., et al., 2002, *A&A*, 390, 81
- [14] Ghirlanda, G., Ghisellini, G. & Lazzati, D., 2004, *ApJ*, 616, 331
- [15] Wang, F. Y. & Dai, Z. G., 2013, *Nature Physics*, 9, 465
- [16] Liang, N., et al., 2008, *ApJ*, 685, 354
- [17] Wang, F. Y. & Dai, Z. G., 2014, *Phys. Rev. D*, 89, 023004
- [18] Yüksel, H., Kistler, M. D., Beacom, J. F. & Hopkins, A. M., 2008, *ApJ*, 683, L5
- [19] Wang, F. Y., 2013, *A&A*, 556, A90
- [20] Hinshaw, G. et al., 2013, *ApJS*, 208, 19
- [21] Fan, X., Carilli, C. L. & Keating, B., 2006, *ARA&A*, 44, 415
- [22] Wang, F. Y., et al., 2012, *ApJ*, 760, 27
- [23] Guidorzi, C., et al., 2015, *ApJ*, 801, 57
- [24] Katz, J. I., 1986, *J. Geophys. Res.*, 91, 10412
- [25] Bak, P., Tang, C. & Wiesenfeld, K., 1987, *Phys. Rev. Lett.*, 59, 381
- [26] Bak, P., Tang, C. & Wiesenfeld, K., 1988, *Phys. Rev. A*, 38, 364